Numerical Analysis of Tidal Turbines using Virtual Blade Model and Single Rotating Reference Frame

Internship performed at: University of Washington

Arthur CERISOLA

From February 27th to August 22nd 2012

Host Director of Research:	Assiociate Professor A. Aliseda
Tutor of Project:	PhD-student T. Javaherchi
Host institute of studies:	Department of Mechanical Engineering - University of Washington, Seattle (WA) - USA
Responsible for Master of Research:	Associate Professor J-A. Astolfi

ABSTRACT

As governments and companies are getting more and more engaged in finding and developing new renewable energy sources, tidal currents have become famous for their high predictability, giving Marine Hydrokinetic (MHK) turbines more and more attention from engineers and researchers. And since the technology involved for building these devices is complex and expensive, CFD simulations have been increasingly used to predict the performances of tidal turbines, still at their early stage of development. This project deals simultaneously with the confirmation of previous results about the optimization of an array of turbines using Virtual Blade Model on FLUENT on one side, and with the behavior of a new MHK turbine geometry, the DOE Reference Model 1, in the near and far wake regions and the calculation of lift and drag coefficients using Single Rotating Reference Frame, on the other side. These two models have completely different levels of accuracy, boundary condition and computational requirements, and thus were applied on two different purposes.

The elaboration of several spacing configurations for an array of 8 turbines, based on semi-empirical data from previous reports about the impact of different parameters on turbines, as to get the best power extraction efficiency, led us to confirm these assumptions through multiple VBM simulations, and the overall efficiency and power output expectations were successfully met.

As for the SRF study, the behavior of the flow field around the blade and in the near wake regions was observed, highlighting the differences between this numerical model and VBM. Besides, the methodology applied to determine the lift and drag coefficients, which are unknown for this geometry and with no experimental data to compare to, and though accuracy for the different angle of attacks along the blade could be improved, gave us a reasonable approximation of these values.

ACKNOWLEDGMENTS

I'd like to thank my supervisor Alberto Aliseda who suggested me this project, made this internship possible and guided me patiently every week throughout my work.
I am heartily thankful to my tutor Teymour Javaherchi, whose every day's advice, encouragement and technical support helped me getting a better understanding of theory and models behind numerical simulations, but also about the philosophy of research.
Special thanks also to Samantha Adamski, who worked by my sides in the lab and made my days at work more entertaining and full of cultural discussions.

Lastly, I'd like to offer my regards to Mr. Deniset and Mr. Astolfi, who connected me to the University of Washington and gave me their encouragements.

TABLE OF CONTENTS

List of figures and tables

1.INTRODUCTION

1.1 TIDAL ENERGY

The global energy requirements are primarily provided by the combustion of fossil fuels. In 2007, the global share of energy from fossil fuels was 88% of the total primary energy consumption. Fossil fuels have powerful but limited potential and, regarding to the current rate of exploitation, it is expected that these resources will deplete within the coming decades. Renewable energy technologies are thus becoming an increasingly favorable alternative to conventional energy sources to alleviate these fossil fuel related issues. (1)

Although wind energy emerged as a leader of new renewable energy sources, other options keep being explored. Recently, the kinetic energy of water currents in oceans, rivers and estuaries has been evaluated and tidal flows have been recognized as a potential opportunity to harvest energy that is renewable and clean. Additionally, unlike many other renewable resources, tidal energy is also very predictable.

Indeed, tides are the cyclic raising and falling of Earth's ocean surface and are caused by the rotation of the earth within the gravitational fields of the moon and sun. Tides change periodically and there are three basic types of tidal patterns, according to a number of interacting cycles:

- A half-day cycle: the rotation of the earth within the gravitational field of the moon, which results in a period of 12 hours 25 minutes between successive high waters.
- Daily tides: only one high tide and one low tide in a 24-hour period.

This is the kind of tide occurring in some regions such as the Gulf of Mexico.

- A 14-day cycle: caused by the superposition of the gravitational fields of the moon and sun. The sun's gravitational field reinforces that of the moon at new moon and full moon and results in maximum tides or spring tides. At quarter phases of the moon, there is partial cancellation, resulting in minimum or neap tides. The range of a spring tide is typically about twice that of a neap tide.

Thus obeying these precise cycles, tidal energy is more predictable, in comparison to other forms of renewable energy, which come from randomly intermittent and variable sources, such as wind or wave.

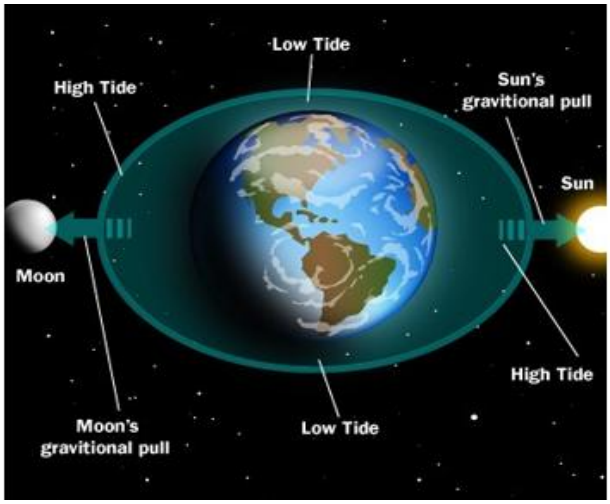

Figure 1.1 : Tidal phenomenon

The power from kinetic energy in these tidally current flows is defined as follows:

$$P = \frac{1}{2}\rho A V^3, \tag{1.1}$$

where ρ is the density of the fluid (i.e. sea water), A is the cross sectional area that the current goes through and V is the velocity of the fluid (i.e. tidal current). Then, an interesting point is that, although the average velocity of tides (2 to 3 m/s) is smaller than the average wind velocity (12 m/s), water is 850 times denser than air and therefore tidal currents have significant energy conversion potential even for relatively slow velocities.

Though harvesting the energy from tidal flows holds many similarities to harvesting the energy in wind, the hydrodynamic application involves new challenges and different physical considerations. Tidal energy industry is still in its beginnings. The technology is where the wind energy industry was approximately three decades ago, with many developments to come (2). And before allowing and launching the production of devices on industrial scale to harvest this energy, much research need to be done to understand the best ways to capture tidal energy efficiently and within a reasonable economically and environmentally range.

There are two main different kinds of MHK turbines: axial flow and cross flow, characterized by the direction of the flow relative to the rotational axis. Because the physics of axial flow turbines are well understood from research and development in the wind industry and are commonly referred to horizontal axis wind turbine (HAWT), axial flow turbines were a logical starting point for research into

marine hydrokinetic turbines.

While the efficiencies of cross flow hydrokinetic turbines (CFHT) are typically less than axial flow turbines (or horizontal axis hydrokinetic turbines – HAHT), cross flow turbines hold certain advantages that may become more pertinent in the hydrokinetic application: ability to operate in shallow waters with an above-water gearbox and electrical generator, ability to operate in channels with very different depth and widths, the opportunity to stack them as to form compact arrays, thus capturing more of the cross section of the flow than possible with a single diameter horizontal axis hydrokinetic turbine, etc. (3)

Figure 1.2 illustrates the two kind of MHK turbines: Cross flow (a) and Axial flow (b & c).

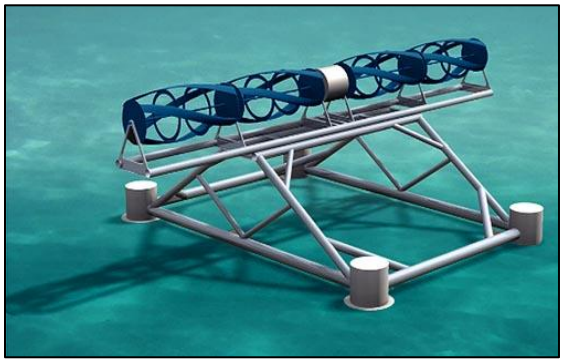

***a**. Ocean Renewable Power Company cross flow turbine*

***b.** Marine Current Turbine SeaGen MHK turbine*

***c**. OpenHydro MHK turbine*

Figure 1.2. Different kinds of MHK turbines (from company websites)

1.2 MOTIVATION AND GOALS

The data used for the first study comes from the National Renewable Energy Laboratory (NREL), which conducted experiments on a two bladed wind turbine, using the S809 airfoil profile, in the NASA Ames wind tunnel (4). Results were made free to access for any researchers, and are considered extremely valuable information for numerical modeling and analysis. The commonly used name for this experiment is NREL Phase VI.

The aim of this first study was to confirm the results and conclusions from the previous reports (5) (6) with an 8 turbines array, including downstream distances, tip to tip distances and lateral offsets, as to have the best configuration for power extraction regarding to the wake effect.

The second study was to evaluate the lift and drag coefficients at different sections of the blade, and near and far wake behavior of a two bladed horizontal axis hydrokinetic turbine (HAHT) designed by the NREL, and officially named DOE Reference Model 1. DOE stands for Department of Energy, an entity which includes the NREL. Since no experimental or numerical data has been established so far, this study could lead to a possible comparison results from a scaled prototype, machined in the NNMREC (Northwest National Marine Renewable Energy Center), University of Washington. This prototype hasn't been tested yet.

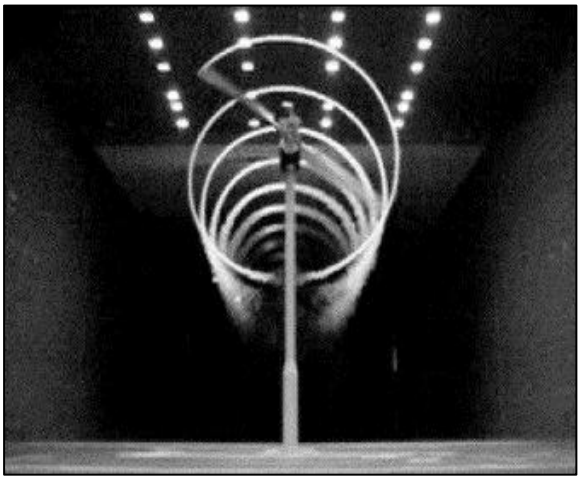

Figure 1.3. Flow visualization with smoke grenade in tip, revealing smoke trails for the NREL turbine in the NASA-Ames

2.NUMERICAL METHODS

2.1 REYNOLDS AVERAGED NAVIER-STOKES , AND TURBULENCE MODEL EQUATIONS OVERVIEW

The NS equations are governing to describe the motion of Newtonian fluids. For a Newtonian and incompressible fluid, the general form of NS equations will be as follows (7):

$$\rho\left(\frac{\partial \mathbf{u}}{\partial t} + \mathbf{u}.\nabla\mathbf{u}\right) = -\nabla p + \mu\nabla^2\mathbf{u} + \mathbf{f}, \tag{2.1}$$

where **u** is the flow velocity vector, ρ is fluid density, p is pressure, μ is dynamic viscosity of the fluid and **f** are forces per unit volume (such as gravity or centrifugal forces)

- $\frac{\partial \mathbf{u}}{\partial t}$ is the unsteady acceleration
- $\mathbf{u}.\nabla\mathbf{u}$ is the convective acceleration (caused by a change in velocity over position)
- $-\nabla p$ is the pressure gradient
- $\mu\nabla^2\mathbf{u}$ is the viscous forces

Since the exact solutions for these equations can't be calculated easily for complex flow fields, such as turbulent flow, different methods have been developed to approximate them. RANS (Reynolds Averaged Navier-Stokes) equations are one of these methods. Based on Reynolds decomposition, these equations are time-averaged:

$$u(x,t) = \bar{u}(x) + u'(x,t), \tag{2.2}$$

where:

- u is a flow variable, such as velocity
- $\bar{u}(x)$ is the mean component, independent upon time
- $u'(x,t)$ is the fluctuating component
- By definition, $\bar{\bar{u}} = \bar{u}$ and $\bar{u}' = 0$

Decomposing **u** and **p** and replacing in (2.1) gives:

$$\rho\frac{\partial\overline{\mathbf{u}}}{\partial t}+\rho\nabla.\overline{\mathbf{u}}\overline{\mathbf{u}}+\rho\nabla.(\overline{\mathbf{u}'\mathbf{u}'})=-\nabla\bar{p}+\mu\nabla^2\overline{\mathbf{u}} \tag{2.3}$$

Thus appears the Reynolds stress term, $-\rho\overline{u_i'u_j'}$, which is a symbol for turbulence behavior, and requires additional modeling to close the RANS equations for solving.

Several RANS-based turbulence models have been introduced during the 20th century adding 1 or 2 equations to provide closure for RANS equations. For this study, only k-ω SST and Spalart-Allmaras models were used as the closure model in numerical simulations.

Spalart-Allmaras model is a one-equation turbulence model that has been developed to remove the incompleteness of algebraic and one-equation models based on k. This model is basically a transport equation for the eddy viscosity as follows:

$$\frac{\overline{D}\upsilon_t}{\overline{D}t}=\nabla\cdot\left(\frac{\upsilon_t}{\sigma_v}\nabla\upsilon_t\right)+S_{v,} \tag{2.4}$$

where the source term S_v depends on the laminar and turbulent viscosities, υ and υ_t; the mean vorticity (or rate of rotation) Ω; the turbulent viscosity gradient $|\nabla\upsilon_t|$; and the distance to the nearest wall, l_w. This model, computationally simpler than two-equation models, has proved successful for aerodynamic flows. However, it has clear limitations as a general model. For example: incapable of accounting for the decay of υ_t in isotropic turbulence, overpredicts the rate of spreading of the plane jet by almost 40% (8)

The k-ω model includes two extra transport equations to represent the turbulent properties of the flow. The first transported variable is turbulent kinetic energy, k, which determines the energy in the turbulence. The second transported variable in this case is the specific dissipation ω and determines the scale of the turbulence. This model is excellent for treating the viscous near-wall regions and for accounting the effects of streamwise pressure gradients. However, the treatment of non-turbulent free-stream boundaries is problematic. Therefore, the k-ω SST (Shear Stress Transport) has been implemented to combine the advantages of both k-ω and k-ε (9).

2.2 VIRTUAL BLADE MODEL (VBM)

The VBM model is the implementation of the Blade Element Momentum theory (BEM) within ANSYS FLUENT, and was originally developed by Zori and Rajagopalan (10) for its application on helicopter rotors. It's a good compromise between the simpler Actuator Disk Model (ADM) and the more complex Single Reference Frame (SRF), which is explained in the next subsection.

The VBM simulates the effect of the rotating blades on the fluid through a body force, which acts inside a disk of fluid with an area equal to the swept area of the turbine. The value of the body force is time-averaged over a cycle from the forces calculated by the Blade Element Method (BEM).

In BEM, the blade is divided into small sections from the root to the tip (see **Figure 2.1**). The lift and drag forces on each section are computed from 2D based on the angle of attack, chord length, airfoil type, and lift and drag coefficient of each segment.

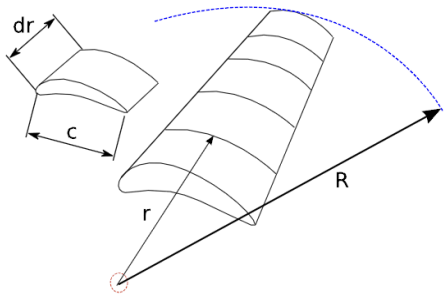

Figure 2.1. Blade element Method

The free stream velocity at the inlet boundary is used as an initial value to calculate the local angle of attack (AOA) for each segment along the blade following:

$$AOA = tan^{-1}\frac{U}{R\omega}, \tag{2.5}$$

where U is the streamwise velocity. Then, based on the calculated values of AOA, lift and drag coefficients are interpolated from a look-up table, which contains values of these variables as a function of AOA, Reynolds number and Mach. With this information, lift and drag forces of each blade element can be calculated by:

$$f_{L,D} = C_{L,D}(AOA, Ma, Re).c_{(r/R)}.\frac{\rho {V^2}_{tot}}{2}, \tag{2.6}$$

where $c_{(r/R)}$ is the chord length, ρ is the fluid density, ${V^2}_{tot}$ is the flow velocity relative to the blade and $C_{L,D}$ the lift and drag coefficients. The chord length and coefficients are needed as inputs for VBM and are usually provided respectively by the manufacturer and the modeler.

Then, these forces are averaged over a full rotation of the blade to calculate the sink term at each cell in the numerical discretization following:

$$F_{L,D_{cell}} = N_b \frac{dr.\mathrm{d}\theta}{2\pi}.f_{L,D,} \tag{2.7}$$

$$\vec{S}_{cell} = -\frac{\vec{F}_{cell}}{V_{cell}}, \tag{2.8}$$

where N_b is the number of blades, r is the radial position of the blade section from the center of the turbine, θ is the azimuthal coordinate and V_{cell} is the volume of the grid cell. The flow is updated with these forces and this process is repeated until convergence is reached.

2.3 SINGLE ROTATING REFERENCE FRAME (SRF)

Generally NS equations are solved, by default, in a stationary (or inertial) reference frame. However there are several problems where it is necessary to solve the equations in a moving (or non-inertial) reference frame. It is still possible to solve them as unsteady problems, but the computational cost will be higher. Such cases usually involve moving parts - like rotating blades, impellers and similar types of moving surfaces. And it is the flow around these parts that is of interest. In most cases, the moving parts render the problem unsteady when observed from the stationary frame. With a moving reference frame, however, the flow can (respecting some conditions) be modeled as a steady-state problem with respect to the moving frame.

For a steadily rotating frame (i.e. the rotational speed is constant), it is possible to transform the equations of fluid motion to the rotating frame so that steady-state solutions are possible. This adds two extra acceleration terms, Coriolis and centripetal acceleration in the momentum equation, and a relation between relative and absolute velocities is needed. (11)

Consider a coordinate system which is rotating steadily with angular velocity $\vec{\omega}$ relative to a stationary (inertial) reference frame, as illustrated in **Figure 2.2.** The origin of the rotating system is located by a position vector $\overrightarrow{r_0}$.

The axis of rotation is defined by a unit direction vector $\hat{a}$ such that

$$\vec{\omega} = \omega \hat{a} \tag{2.9}$$

The computational domain for the CFD problem is defined with respect to the rotating frame such that an arbitrary point in the CFD domain is located by a position vector $\vec{r}$ from the origin of the rotating frame. The fluid velocities can be transformed from the stationary frame to the rotating frame using the following relation:

$$\overrightarrow{v_r} = \vec{v} - \overrightarrow{u_r} \tag{2.10}$$

With $\overrightarrow{v_r}$ the relative velocity, $\vec{v}$ is the absolute velocity (the velocity viewed from the stationary frame), and $\overrightarrow{u_r}$ is the "whirl" velocity (the velocity due to the moving frame):

$$\overrightarrow{u_r} = \vec{\omega} \times \vec{r} \tag{2.11}$$

The equations of motion can be expressed in two different ways:

- Expressing the momentum equations using the relative velocities as dependent variables (known as the relative velocity formulation).

- Expressing the momentum equations using the absolute velocities as dependent variables (known as the absolute velocity formulation).

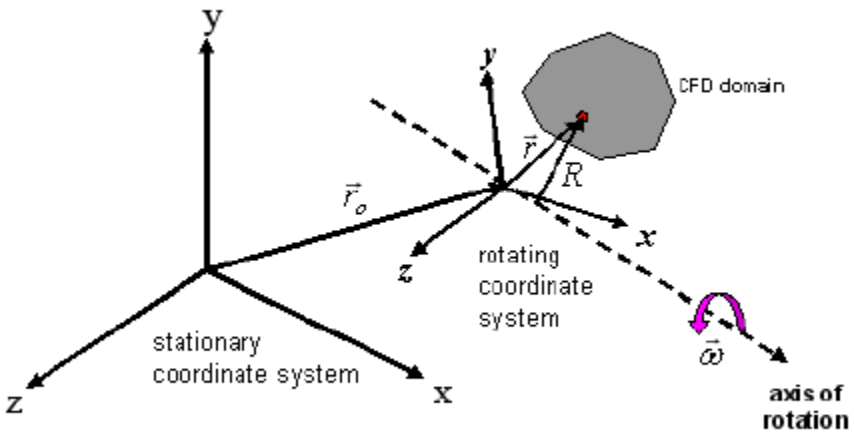

Figure 2.2. Computational domain, stationary (absolute) and rotating (relative) reference frames

Relative velocity formulation

Conservation of mass:

$$\frac{\partial \rho}{\partial t} + \nabla \cdot \rho \overrightarrow{v_r} = 0 \tag{2.12}$$

Conservation of momentum:

$$\frac{\delta}{\delta t}(\rho \overrightarrow{v_r}) + \nabla \cdot (\rho \overrightarrow{v_r} \overrightarrow{v_r}) + \rho(2\vec{\omega} \times \overrightarrow{v_r} + \vec{\omega} \times \vec{\omega} \times \vec{r}) = -\nabla p + \nabla \cdot \overline{\overline{\tau_r}} + \vec{F} \tag{2.13}$$

Conservation of energy:

$$\frac{\delta}{\delta t}(\rho E_r) + \nabla \cdot (\rho \overrightarrow{v_r} H_r) = \nabla \cdot (k \nabla T + \overline{\overline{\tau_r}} \cdot \overrightarrow{v_r}) + S_h \tag{2.14}$$

With $(2\vec{\omega} \times \overrightarrow{v_r})$ the Coriolis acceleration term, $(\vec{\omega} \times \vec{\omega} \times \vec{r})$ the centripetal acceleration term, $\overline{\overline{\tau_r}}$ the

viscous term. Moreover, the relative internal energy (E_r) and the relative total enthalpy (H_r) used in the energy equation are defined as:

$$E_r = h - \frac{p}{\rho} + \frac{1}{2}(v_r^2 - u_r^2) \tag{2.15}$$

$$H_r = E_r + \frac{p}{\rho} \tag{2.16}$$

Absolute velocity formulation

Conservation of mass:

same as (2.12)

Conservation of momentum:

$$\frac{\delta}{\delta t}(\rho\vec{v}) + \nabla \cdot (\rho\overrightarrow{v_r}\vec{v}) + \rho(\vec{\omega} \times \vec{v}) = -\nabla p + \nabla \cdot \bar{\bar{\tau}}_r + \vec{F} \tag{2.17}$$

Conservation of energy:

$$\frac{\delta}{\delta t}(\rho E) + \nabla \cdot (\rho\overrightarrow{v_r}H + \rho\overrightarrow{u_r}) = \nabla \cdot (k\nabla T + \bar{\bar{\tau}} \cdot \vec{v}) + S_h \tag{2.18}$$

In this formulation, the Coriolis and centripetal accelerations can be collapsed into a single term ($\vec{\omega} \times \vec{v}$).

This is the way SRF is modeling the flow field.

3.IMPLEMENTATION OF NUMERICAL METHODS

3.1 PREVIOUS RESULTS

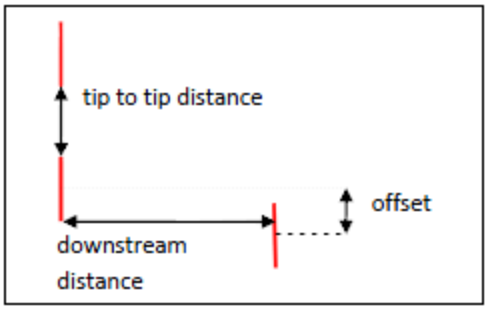

Figure 3.1. Main parameters for VBM study

This section summarizes the work of previous studies on MHK turbine array optimization (5) (6). **Figure 3.1** defines the parameters used in the simulations and meshing: tip to tip distance is the distance between the tip of a turbine's blade and another turbine's blade, the offset is the distance between two axis of rotation and the downstream distance between two planes of rotation.

In the previous works array optimization studies has been done via the VBM to show the different impacts of the above parameters on the power extraction as to find an optimal arrangement for an array of tidal turbines. Besides, as VBM is effective enough to evaluate the far wake effect, the studies focused on the influence of the wake of upstream turbines on downstream ones, thus considering the power they can extract. The main data used for the current study are presented below.

Table 3.1 shows the necessary downstream distance to recover X% of the initial extracted power by the upstream turbine, with no offset distance. Then, 87 radii distance from the upstream distance would be needed if we want the downstream turbine to extract the same amount of power as the other one.

Table 3.1. Downstream distance versus power

Percentage of initial power	Distance d (Radius)
100%	87
95%	64
90%	46
85%	33
80%	23
75%	16
70%	10

Figure 3.2 highlights the impact of offset and tip to tip distances on power extraction. It considers a fixed downstream distance of 8 radii from two aligned upstream turbines. These results show that increment

in offset between up- and downstream turbines will increase the amount of power extracted by downstream device. The reason behind this gain of power is avoiding the wake of upstream turbine and receiving inflow with higher amount of kinetic energy.

The extracted power by downstream turbine increase more for a negative offset compared to the same positive offset. This is due to an acceleration of the flow beween the two upstream turbines, as a negative offset brings the third one between the two upstream.

Finally, the extrapolated value of the normalized power extracted with no offset distance (~60%) makes sense with **Table 3.1** since we are at 8 radii downstream distance.

More combinations of the three parameters and resulting data can be seen in (5) (6).

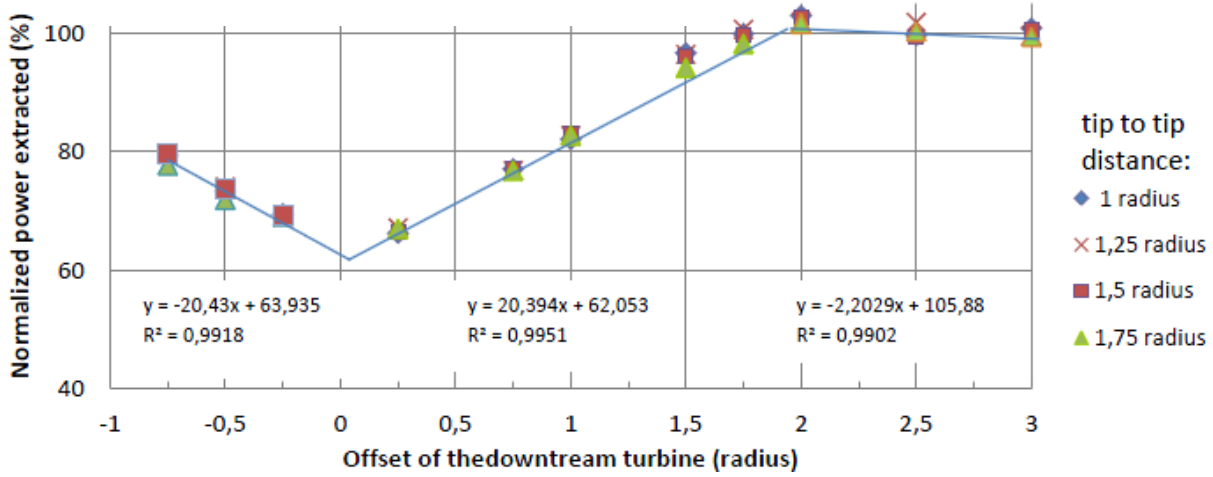

Figure 3.2. Normalized power extracted by an 8 radii downstream distance turbine

Different profiles of inlet velocity were also tested as to observe the impact of the seabed on the average flow velocity (boundary layer effect, potential sedimentation) but only a constant uniform velocity has been used for this study.

3.2 VBM

Different configurations

Based on the numerical results from the previous reports, an array of 8 turbines has been set to aim the best overall power extraction efficiency within reasonable working areas, using the 3 different parameters. It has been decided to arrange this array on 3 rows, each of them containing 2 or 3 turbines. Considering this criterion, two different "patterns" have been tested. Both have a tip-to-tip distance of 2 radii for the 2 first rows.

The first one, named "aligned", has its 3rd row turbines aligned with upstream turbines in the first row, and the turbines from the second row have a lateral offset of 2 radii, thus avoiding a direct wake effect. The downstream distance between the rows was fixed at 8R then 4R.
The second pattern, named "staggered", has its 2nd row staggered with a lateral offset of 1.5R from the first row, and the 3rd row with 1.5R from the second as well. The downstream distance between the rows was fixed at 8R then 4R.
The two patterns are shown on **Figure 3.3.** The aligned one is in black and the staggered in green.

Dimensions

The channel has a rectangle cross section, and its dimensions are 400m X 122m X 50m (∼75R X 22R X ∼9R). The first row of turbines is located 4R downstream the inlet and more than ¾ of the total length of the channel are needed for the wake behavior to be solved and converged by Fluent.
The disks modeling the turbines are 5.54m radius, respecting the same dimensions as the NREL turbine, and are located 15m from the seabed.
The width of the channel has been set as to avoid any wall effect inducing acceleration of the flow, and possible variation of velocity values on the side turbines.

Boundary Conditions and Solving information

Table 3.2 shows a summary of boundary condition and numerical scheme used in simulations for array optimization.

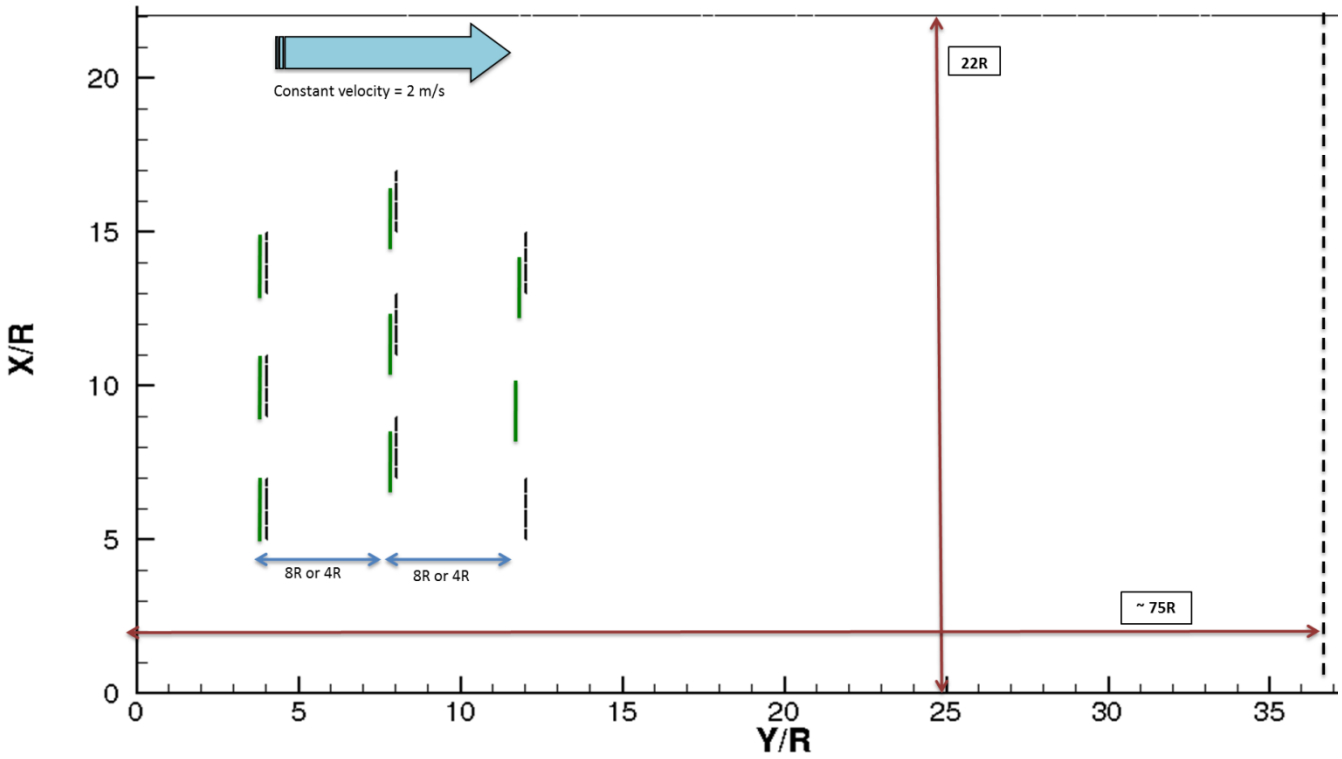

Figure 3.3. Different configurations of the turbine array: Staggered (green) and Aligned (black). R is the radius (5.53m) of a turbine. View from top (XY plan).

Table 3.2. General solving information for VBM

Mesh size	4.5 million elements
Meshing method	Hex/Wedge Cooper and Tet/Hybrid
Number of Iterations	~ 700
Turbulence model	$k-\omega\ SST$
Inlet Boundary Condition	Velocity Inlet 2 m/s
Outlet Boundary Condition	Pressure Outlet
Walls Boundary Condition	Velocity Inlet 2 m/s
Pressure-Velocity Scheme	SIMPLE
Discretization of Gradient	Green-Gauss Cell Based
Discretization of Pressure	Second Order
Discretization of Momentum	QUICK
Turbulent Kinetic Energy	QUICK
Specific Dissipation Rate	QUICK

UDF in Fluent

A user-defined function (UDF) is a C-programmed function that can be dynamically loaded with the FLUENT solver to enhance the standard features of this CFD commercial package. For example, a UDF can be used to define special boundary conditions, material properties, and source terms for flow regime, as well as specify customized model parameters (ex: multiphase models), initialize a solution, or enhance post-processing. (12)

The VBM is limited to 20 different segments for a rotor, and 10 rotors maximum per case of study. However, the code is free to be modified, with respect to the UDF structure.

Figure 3.5 shows the different inputs to set as to run the VBM in FLUENT, concerning the general information about the blades such as radius, number of blades, angular velocity, the origin of the rotor disk. All these information are based on NREL phase VI turbine experimental data.

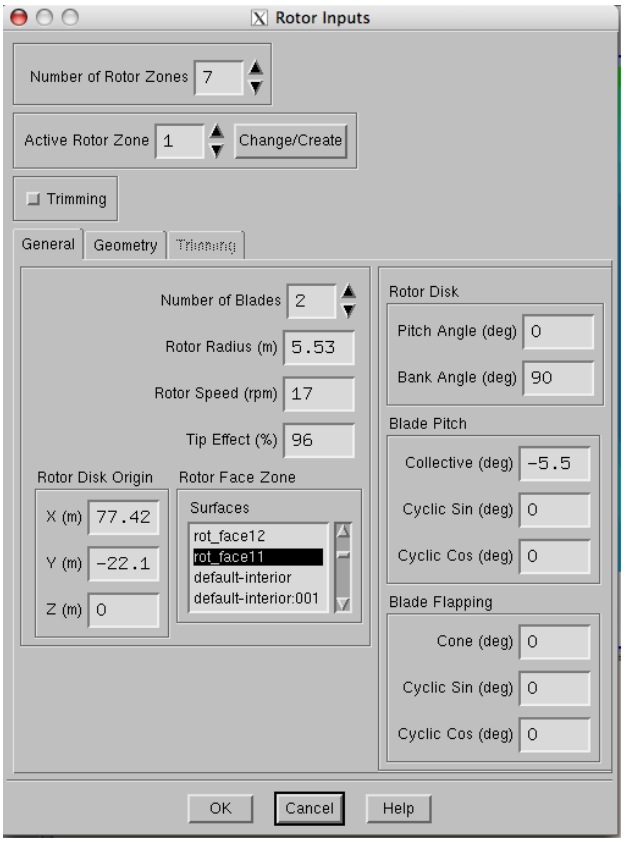

Figure 3.5. VBM general control panel

Figure 3.4 displays the geometrical information about the 20 different blade segments, such as relative radial position, chord, local twist angle, and a look-up table for the lift and drag coefficients for each segment from a file (S809). This table contains the coefficients as a function of angle of attack, Reynolds and Mach number. Then after each iteration, new values of AOA, lift and drag forces and power will be computed for each segment until convergence is reached.

See **Appendix A** for more information about the geometry of the NREL phase VI blade.

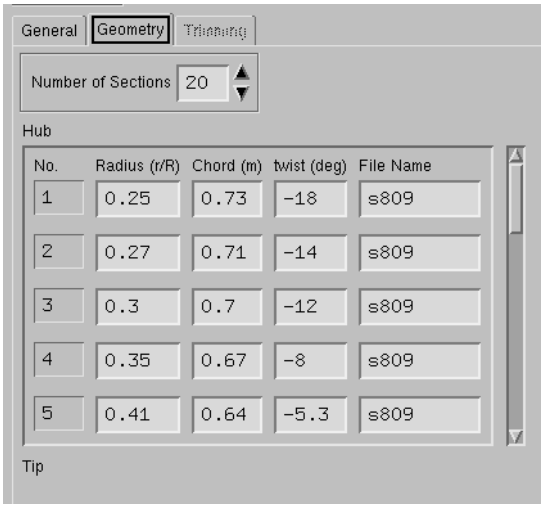

Figure 3.4. VBM geometry control panel

3.3 SRF

Since the VBM averages the hydrodynamic effects of the blade over the whole disk area, it doesn't capture the details of the flow right behind the turbine. SRF, on the contrary, has such capabilities, and can also be used to compute the different forces applied to the blade as to determine lift and drag coefficients.

Geometry of the blade (see Appendix B)

The blade geometry modeled using SRF model is called DOE Reference Model 1. This blade design has been developed and optimized in National Renewable Energy Laboratory (NREL) in US. The distance from axis of rotation to tip is 10 meters. However, not the whole blade was meshed for SRF simulation, as the lower part was more a connection to the hub than a lift-generating section.

Mesh

Starting with importing the blade geometry from SolidWorks to Gambit, the mesh was structured around it. First, the blade was split in 27 volumes (see **Figure 3.7**), to compute different forces independently from each other on FLUENT later. Then a C-mesh is created around it as to keep a control on the near-wall regions, where the turbulent boundary layer will be developed. Wall function approach was used in order to get an accurate representation of the flow field in this region, which is necessary to predict the overall behavior of the turbulent flows (**Figure 3.6** The wall function approach uses a semi-empirical formula to solve the equations in the viscous sublayer and buffer layer (the viscous-affected regions) instead of having a more refined mesh at the wall. Therefore, it saves time and computational resources compared to the near-wall model Approach, and staying reasonably accurate to predict the mean velocity profiles, flow detachment, dissipation mean shear at the wall, etc.

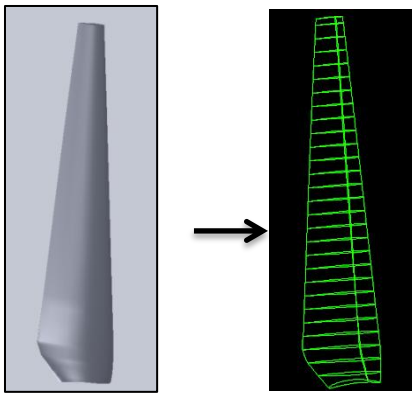

Figure 3.7. From SolidWorks to Gambit

As to use properly these Wall Functions, each wall-adjacent cell centroid should be located

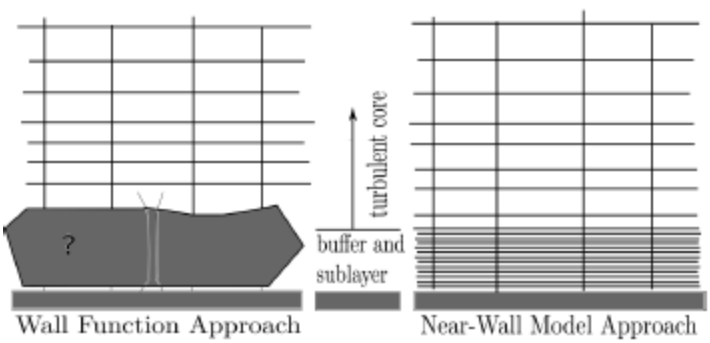

Figure 3.6. Two approaches for near wall region meshing

approximately within the log-law layer $30 < y^+ < 300$, y^+ being defined as:

$$y^+ = \frac{u_\tau y}{\upsilon}, \tag{3.1}$$

where y is the nearest distance to the wall, υ is the kinematic viscosity of the fluid and u_τ is the friction velocity, defined as:

$$u_\tau = \sqrt{\frac{\tau_w}{\rho}}, \tag{3.2}$$

with τ_w the friction stress at the wall.

Considering the range chosen for this case, the following estimation of y^+ can be made:

$$y^+ = \sqrt{\frac{\rho u y}{\mu}}, \tag{3.3}$$

where u is the relative velocity at the corresponding section of the blade (composition of free stream velocity and tangential velocity). Consequently, the value of the nearest distance to the blade wall can be calculated, knowing the extreme values of y^+, and was set slightly differently between sections around the root and sections close to the tip. But since the mesh around each section is uniform, and because the friction velocity is not, it is difficult to keep y^+in the 30-300 range everywhere.

FLUENT provides a display for y^+as a function of X-position (close to the chord line) as shown on **Figure 3.8** and was a way to check the resolution of the SRF mesh close to the blade walls, from the root to the tip. Below are displayed 3 different sections of the blade.

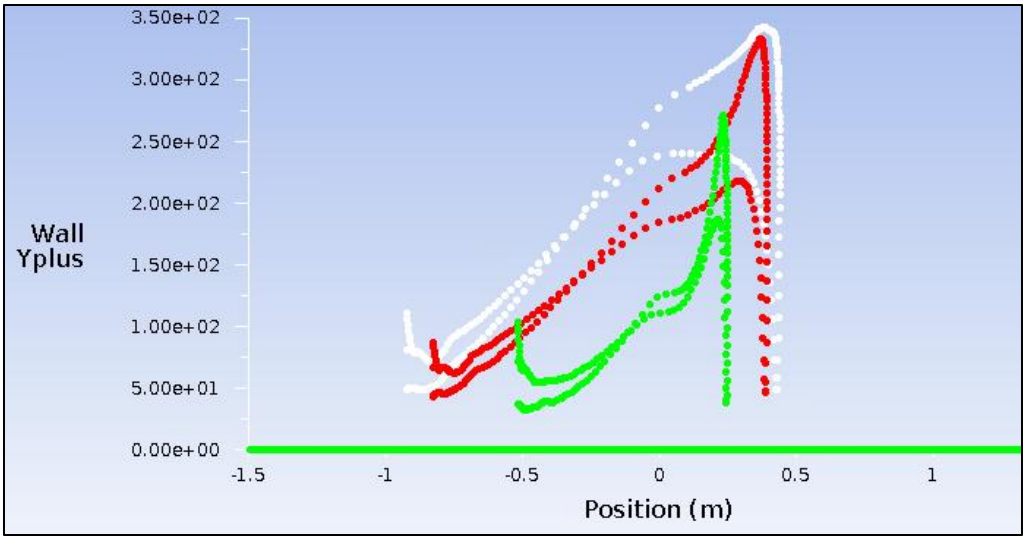

Figure 3.8. y+= f(x) in ANSYS Fluent for the studied case (from top to bottom: at Radius = 5m, 6m, 9m)

Boundary Conditions and operating conditions

The SRF model, on the contrary to VBM, needs an axisymmetric domain to operate, which means for example that a shear velocity profile at the inlet can't be used to simulate the effect of the bottom of the channel on the flow, closer to reality. Also, a semi-circular cross section was chosen to respect this axisymmetric condition, and the half-hub of the turbine was extended to the whole length of the domain. **Figure 3.9** shows the main channel dimensions and boundary conditions.

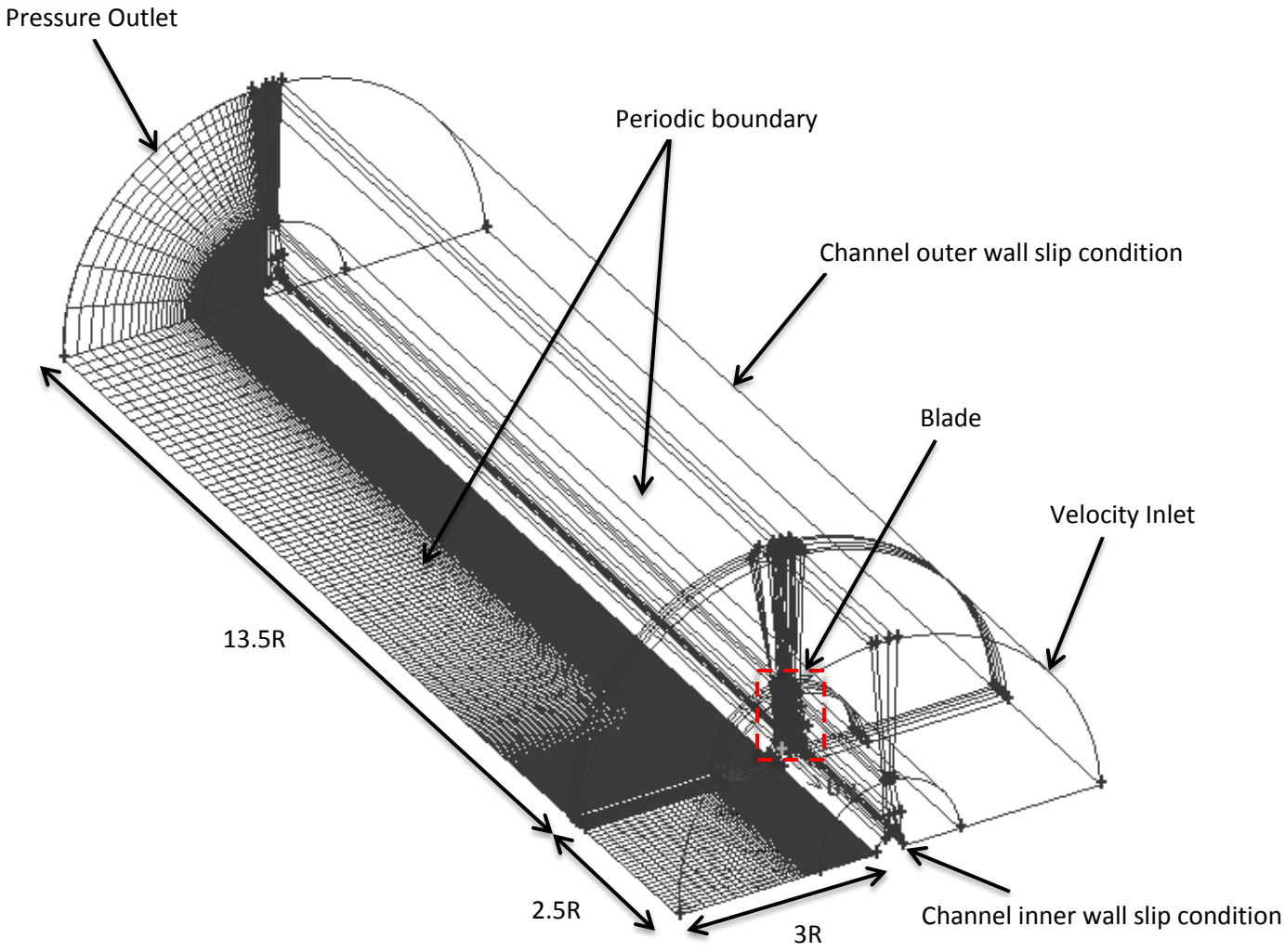

Figure 3.9. SRF domain and boundary conditions

Regarding to the channel inner and outer wall, the boundary conditions have to be set to wall, with the option of Moving Walls Relative to the Adjacent Cell Zone with a rotational speed of 0 rpm (13). Indeed, using the SRF model implies setting a Rotating Reference Frame, which is defined by the periodic

boundary conditions. Then the flow is rotating in the absolute frame, but fixed in the relative frame. And so are the walls: If relative velocities are specified, a velocity of zero means that the wall is stationary in the relative frame, and therefore moving at the speed of the adjacent cell zone in the absolute frame. **Figure 3.10** displays the toolbox to use for these settings in FLUENT.

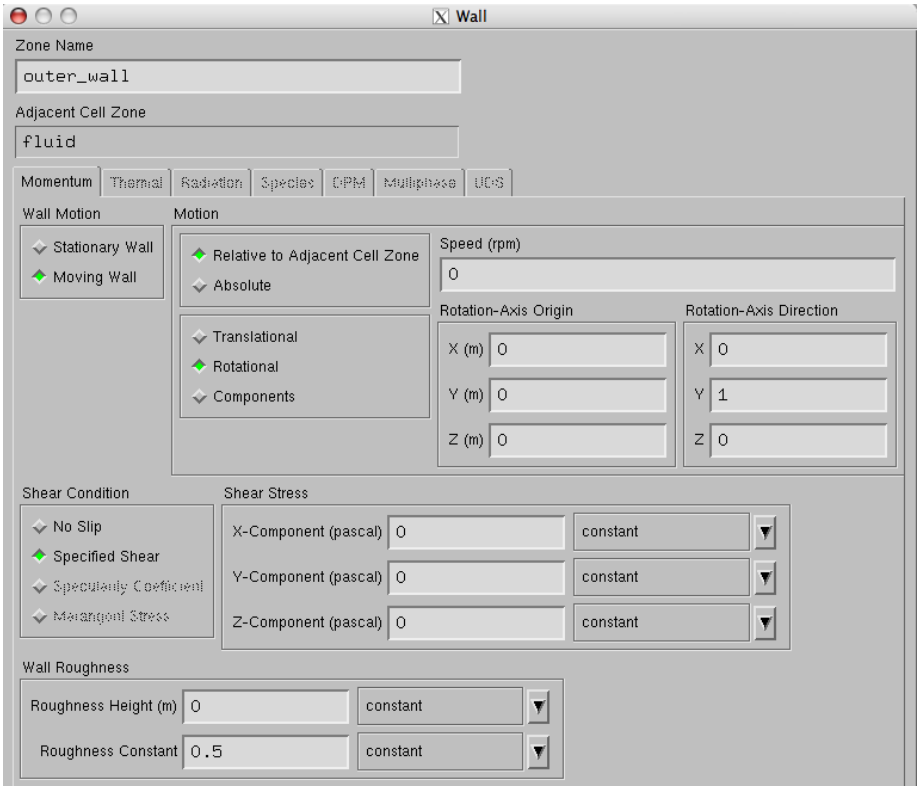

Figure 3.10. Wall boundary condition in FLUENT

In order to get a stable and converged solution at the desired operating conditions, the rotational speed of the turbine had to be gradually increased. In this way, the rotation of the reference frame and the motion induced by the boundary conditions will not lead to large complex forces in the flow as the angular velocity increases. Moreover, since the angle of attack depends on the free stream and angular velocities, this increment will avoid any large angle of attacks that would cause flow separation along the blade and non-physical results. In this case, as to reach a free stream velocity of 2 m/s and an angular velocity of 1.4 rad/s, two intermediate steps with lower operating values were realized, which led to an important number of iterations (see **Table 3.3**)

Table 3.3. General solving information for SRF

Mesh size	~ 10 million elements
Meshing method	Hex/Map (Structured)
Number of Iterations	~16000
Turbulence model	Spalart-Allmaras
Inlet Boundary Condition	Velocity Inlet 2 m/s
Rotational speed	1.4 rad/s
Outlet Boundary Condition	Pressure Outlet
Walls Boundary Condition	Moving Wall
Pressure-Velocity Scheme	SIMPLE
Discretization of Gradient	Green-Gauss Node Based
Discretization of Pressure	Second Order
Discretization of Momentum	QUICK
Discretization of Turbulent Viscosity	Second Order Upwind
Pressure Under-relaxation Factor	0.2
Momentum Under-relaxation Factor	0.6
Modified Turbulent Viscosity Under-relaxation Factor	0.6

Results and post-processing operations are presented and discussed in **4.2.**

4.RESULTS

4.1VBM: CONFIRMATION OF PREVIOUS REPORTS

General behavior

Simulations were run for the different staggered and aligned configurations (see **3.2**), since the two arrays were expected to have the same performances for extracting power for other turbines' wake.

Figure 4.1 highlights both configurations with a 4 radii downstream distance bewteen each row. The view is a plan cut at the origins of the turbines (z=0m). X axis, Y axis and velocity magnitude are adimensionalized with the radius of the turbine and the free stream velocity (2m/s) respectively.
The axisymmetric behavior, assumed by VBM, can be observed in the wake of the turbines. However, contrarily to SRF, all phenomena happening in the near wall region can't be seen (vortex shedding, tip vortices etc.), but this wasn't the focus point of this study.
Right before the blade (upstream), a velocity deficit occurs as the flow arriving on the turbines is affected by their rotation. Moreover, the flow is slightly accelereting (up to 5% faster) around the tips of the blades due to the reduction of the cross-section area. This acceleration, though, may affect the performances of the second row of turbines, and will be analysed further down.

Table 4.1 presents the data analysed and compared in the VBM study. The Thrust, Torque, Power, Minimum and Maximum Angle of Attacks were all reported by the VBM. The available power is the power from the kinetic energy, defined in **Equation (1.1)**, and the V^3 term used is the velocity extracted from a plane located 2 radii upstream each turbine. The distance 2R is based on previous analysis. It was showed that 2R upstream of the device the rotation of the blades are not affecting the flow significantly. To get this value, a customizable script was run on the software Tecplot, which extract a plane 2R upstream each turbine and then get the orthogonal projection of the rotor disk, and average the values of x-y-z velocities before calculating the final velocity magnitude. See **Figure 4.3.** What is called "Local Efficiency" is the ratio Power/Available Power for each turbine. Considering this parameter, the Staggered configuration appears to be slightly more efficient than the other.

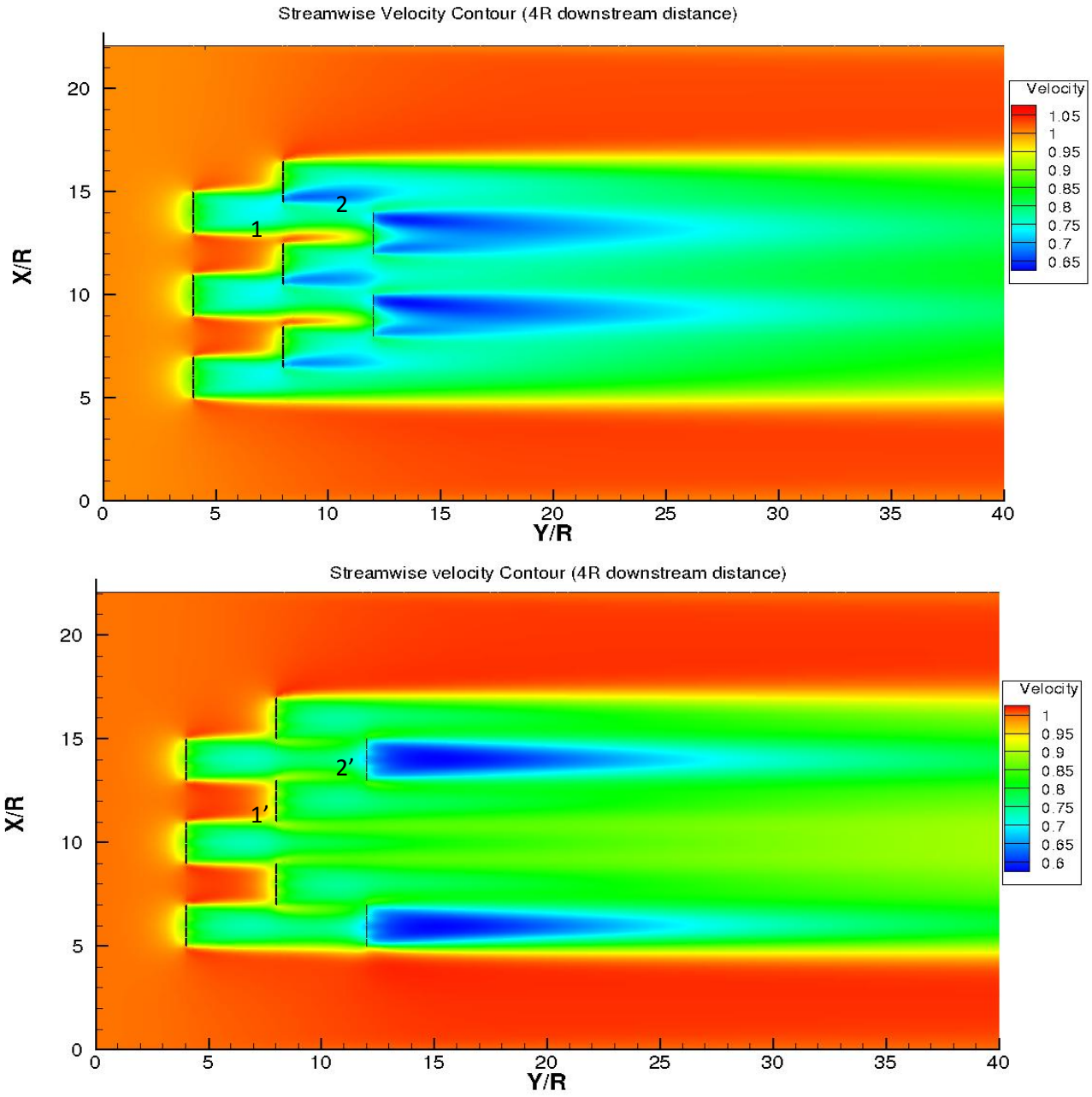

Figure 4.1. VBM velocity contours for both staggered and aligned configurations

Table 4.1. Example of results after VBM simulation for different turbines

	Thrust (kN)	Torque (kN.m)	Power (kW)	Minimum AOA (°)	Maximum AOA (°)	Available Power (kW)	Local Efficiency (%)
Turbine 1	76,87	56,24	100,12	4,78	11,62	342,29	29,25
Turbine 1'	79,83	60,11	107,02	6,35	11,66	397,86	26,90
Turbine 2	69,10	46,08	82,04	4,64	10,32	279,85	29,32
Turbine 2'	61,18	36,24	64,51	5,1	7,67	227,93	28,30

Interpretation and comparison

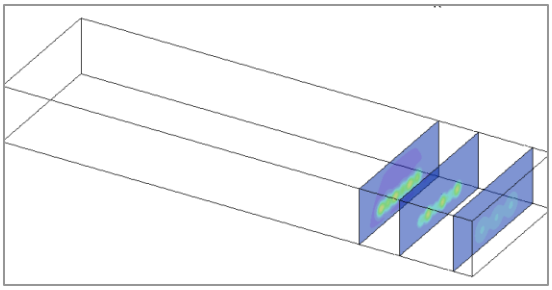

Figure 4.3. Data extraction from orthogonal planes on TecPlot

- Turbine 1 extracts ~7% less power than 1' due to 1.5R lateral offset of the second row in the staggered arrangement, whereas Turbine 1' seems not to be affected at all by the wake from the first row turbines, being 2R offset, in the aligned arrangement. Indeed, power records from the first row of turbines (in both arrangement) have the same order of magnitude (105-107 kW). However, the acceleration induced by the rotation of the two turbines upstream could also have an impact on the extracted power by 1'. Other simulations were performed to confirm or not this impact. See **Figure 4.2.**

- Turbine 2' extracts ~27% less power than 2, thus being more sensitive to the wake of the coaxial turbine upstream.

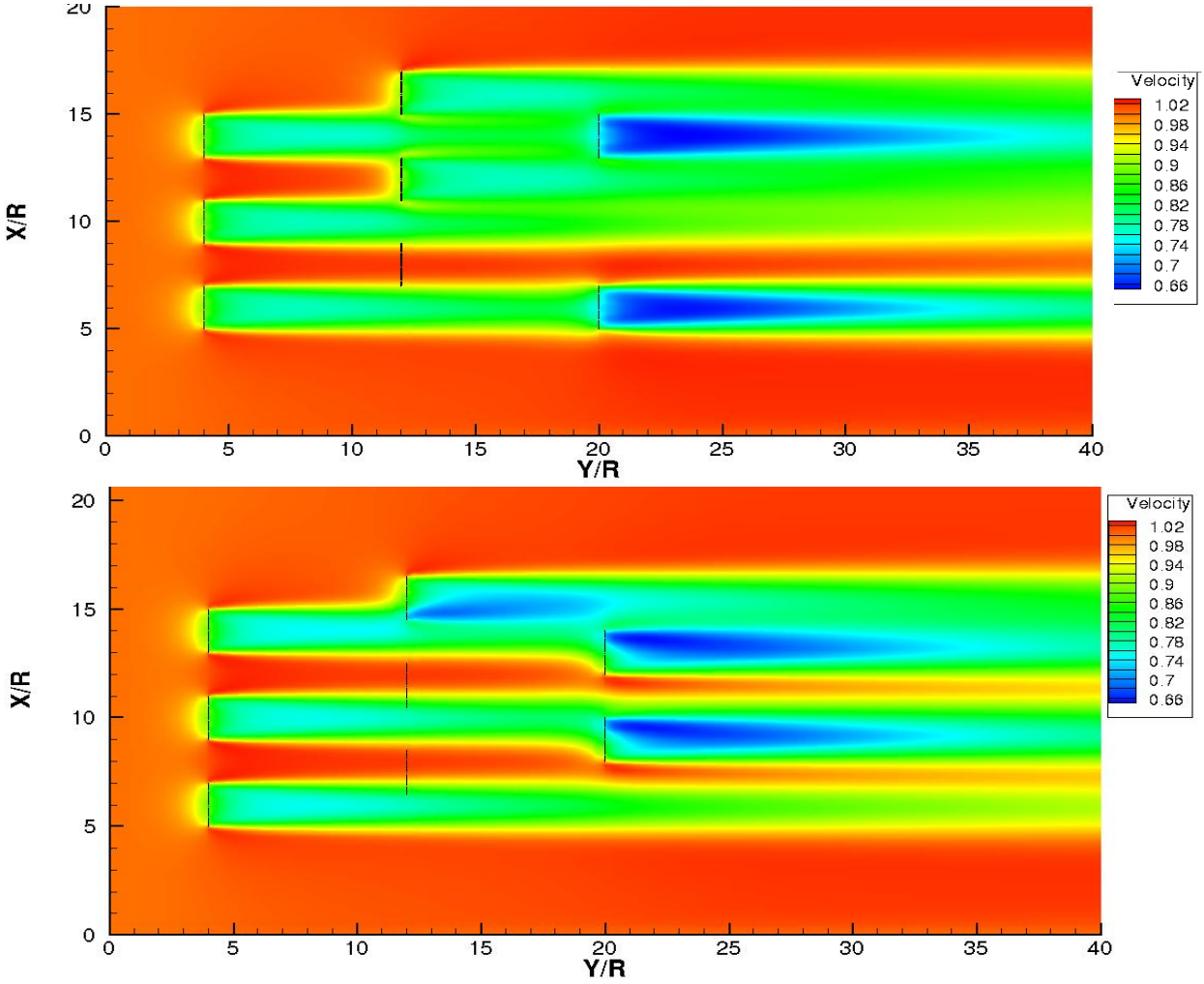

Figure 4.2. VBM velocity contours for both configurations without 1 or 2 turbines

As illustrated in **Figure 4.2**, several simulations with different combinaisons of disabled turbines have been performed on both configurations, and with both 8R and 4R downstream distances, to see the possible interactions between the wakes. It turned out that with a 2 radii lateral offset, downstream turbines are not affected by the upstream one, regarding to power extraction. For example, on the top **Figure 4.2**, one turbine has been disabled. Data analysis shows that wether it is activated or not, its wake doesn't change the extracted power of the turbine downstream, with a 2R lateral offset. Then, the slight acceleration has definitely no improvement effect on the power extraction of the second row, also due to the rapidity of mixing of the flow. Same kind of reasoning was done with the staggered configuration to confirm previous expectations.

Figure 4.4 presents the total extracted power in kW by the 8-turbines array for staggered and aligned configurations, with 2 different downstream distances, and the total power that was predicted using the different empirical results from previous reports. It appears that the expected amount of power meets the data computed by VBM with more than 97% accuracy. Therefore, it confirms the reliability of these reports for any array of turbines modelized with VBM on FLUENT.

Besides, wether regarding to the area covered by the array or not, the staggered configuration is likely to be more effective for power extraction than aligned.

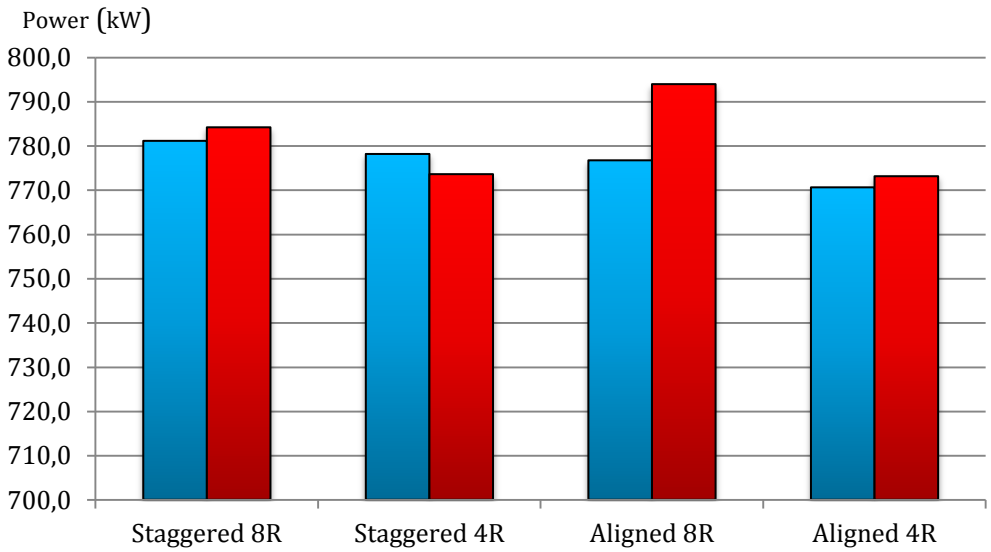

*Figure 4.4. **Overall Calculated Power via VBM** vs **Estimated Power using previous reports***

Figure 4.5 shows the limited streamlines and the relative pressure contours on the suction side of the blade with a Reynolds Number of 2.10^6 and a Tip Speed Ratio (T.S.R) of 7, where:

$$T.S.R = \frac{\omega R}{U_\infty} \tag{4.1}$$

with R the radius of the blade, ω the angular velocity and U_∞ the free stream velocity.

The design of the geometry and operating conditions were chosen to avoid cavitation at the tip and flow separation along the blade at a certain depth. Considering the values of the pressure contours, cavitation is likely to be avoided if the turbine is set at least few meters away from the surface, since the saturated vapor pressure of water at 20°C is ~2300 Pa (at the surface) and that there's a depression zone of almost -1 atm.

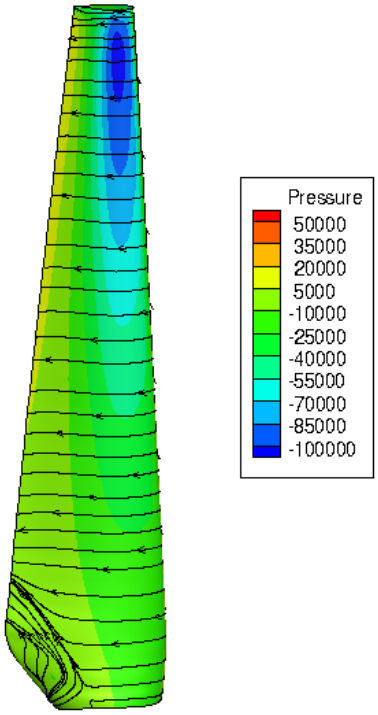

Figure 4.5. Limited streamlines and pressure contours of the SRF blade.

Flow separation (= the fluid flow becomes detached from the surface of the object, and instead takes the forms of eddies and vortices) can be observed at the root, where the streamlines are diverging from their straight path. The other converging lines are a sign of a recirculation zone on the suction side. The reasons of this separation are first that the profiles in this zone have more an elliptical shape than for the rest of the blade, and also because the values of angle of attack are high ($(10° < AOA < 15°)$. This separation, inducing vortices, had a negative effect on the convergence speed of simulations (requiring around 15000 iterations) and the values of the continuity residuals when monitoring on FLUENT (only reaching about 3.10^{-2}).

Figure 4.6 illustrates the impact of the separation on the wake of the blade by displaying the vorticity magnitude (/s) on a X=0 cut plane, where vorticity is defined as the curl of velocity:

$$\vec{\omega} = \vec{\nabla} \times \vec{u} \tag{4.2}$$

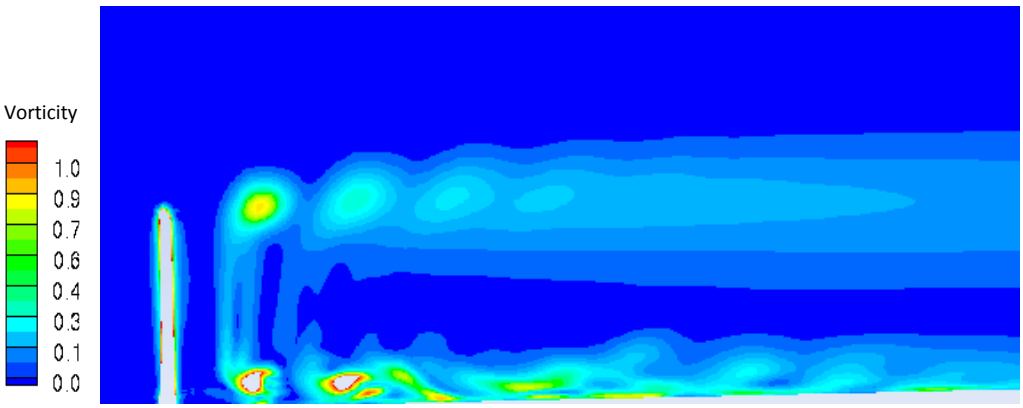

Figure 4.6. Vorticity magnitude (/s) on FLUENT (X=0 cut plane)

Figure 4.7. Scaled prototype of the DOE Reference model 1

Two phenomena can be observed: strong vortex shedding at the lower wall and tip vortices behind the tip of the blade.

Vortex shedding is explained by the geometry of the blade around the hub, shown on Erreur ! Source du renvoi introuvable.. It was based more on structural issues (as to get built and assembled more easily) than hydrodynamic issues (as to have better hydrodynamic performances), and lead to elliptical shapes at the root. And also because the root area of the turbine doesn't contribute much to the overall torque (R is small) (see 4.3).

This turbulent and unsteady phenomenon was also the cause for high continuity residual value on FLUENT monitors and the impossibility to get a fully converged solution. However, these vortices are dissipating after few radiuses downstream, quickly mixing with the flow, and don't affect the overall performances of the turbine since at a low radius, the high value of angle of attack leads to low values of lift coefficients and high values of drag coefficient.

Figure 4.6 also shows several circular shapes whose vorticity magnitude is progressively decreasing as the flow goes downstream. Those are tip vortices, which follow an helicoidal path, whose angle is linked to the TSR and the diameter of the blade. **Figure 4.8** describes the general phenomenon for a 3 bladed turbine (14)**.**

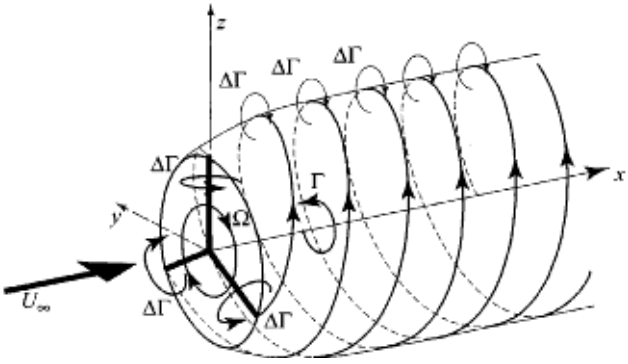

Figure 4.8. Helical vortex wake shed by rotor with three blades each with uniform circulation $\Delta\Gamma$

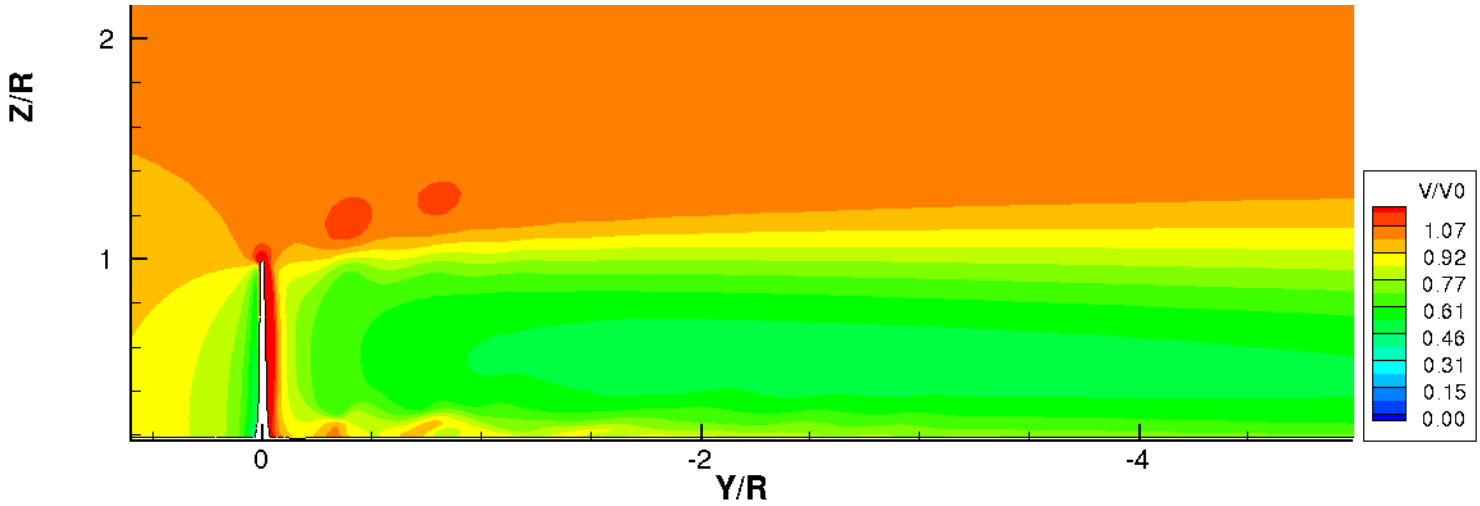

Figure 4.9. Normalized Velocity Magnitude Contours in the near wake region of the blade, X=0 cut plane.

Tip vortices are also illustrated on **Figure 4.9,** as circular accelerated zones, and the wake expansion can be noticed as the second tip vortex is located higher than the one closest to the blade. The vortices shed at the root are visible as small accelerated zones as well, but dissipate within 2 radiuses downstream.

Figure 4.10 show the behavior of the flow on the turbine, in the form of the normalized velocity magnitude, at different Y-cuts planes along the channel, from upstream to downstream (looking from left to right then top to bottom). At Y/R=-0.05 (50cm) upstream to the blade, the flow starts to be affected by the downstream rotation, and is no longer axisymmetric. At Y/R=0 and 0.05, the suction side presents a strong deceleration of the velocity magnitude (up to 70% of the initial speed), except at a small spot located at the root, linked to the shed vortices and the flow separation. The acceleration zone induced by the tip slowly moves and expands as the flow goes downstream (Y/R=1 and Y/R=1.5) and becomes axisymmetric again. At Y/R=1.5, the wake has expanded to its maximum range and the velocity deficit is still important in the inner zone. At Y/R=10 (100m) downstream the blade, the flow continues its mixing and the original velocity of 2m/s is slowly recovering all the area.

Tip and root vortices and other phenomena which are non-axisymmetric related can't be seen if using VBM or ADM. For more comparisons of these 3 models, see (15).

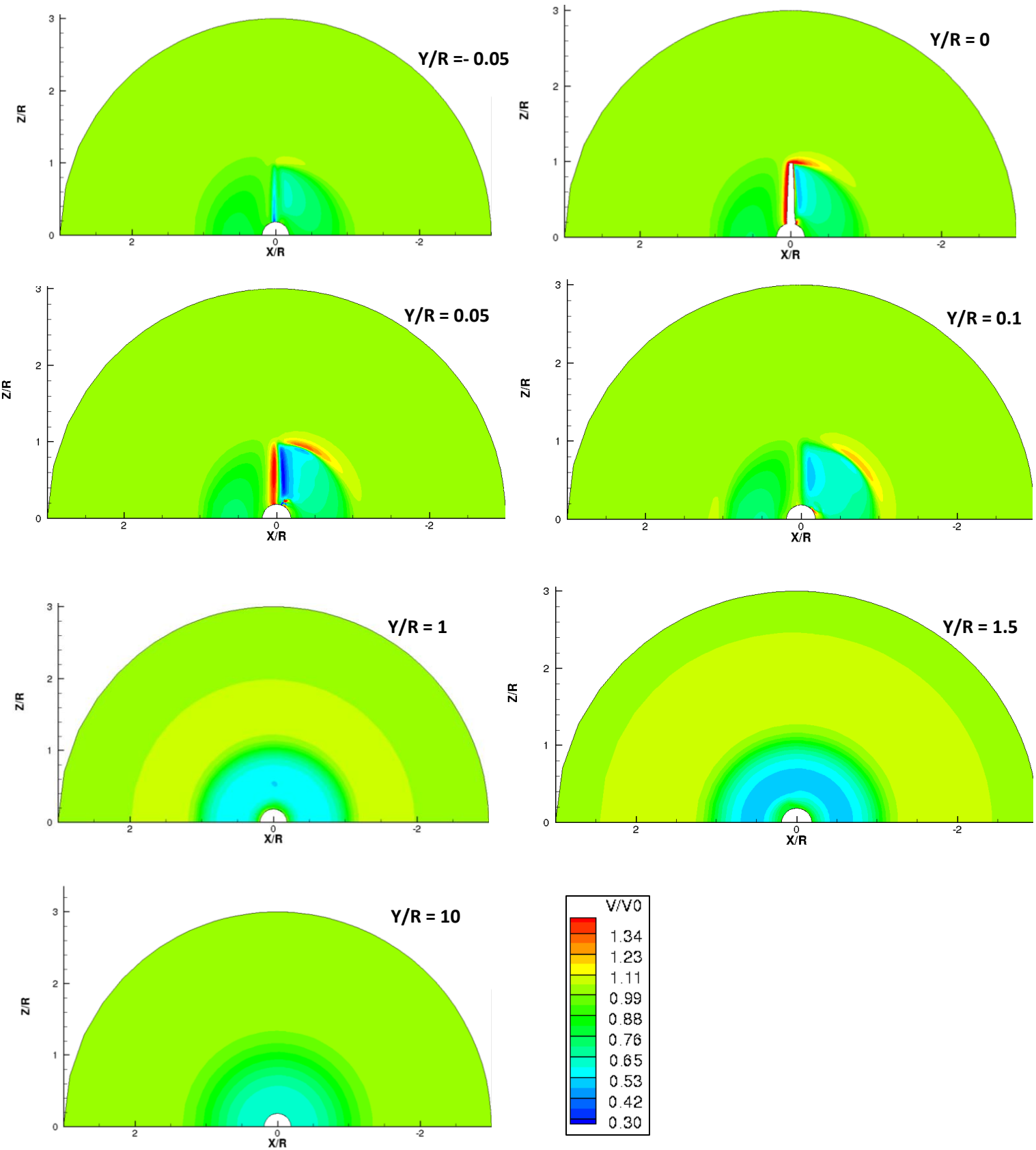

Figure 4.10. Normalized velocity contours on Y-cuts planes along the tidal channel

4.3 SRF: LIFT AND DRAG COEFFICIENTS

Methodology

The following methodology has been applied to evaluate the lift and drag coefficients from data extracted from ANSYS FLUENT.

1/ Using the Report→Forces tool in FLUENT, with direction vector of (1,0,0) and (0,-1,0) respectively to get the force perpendicular and parralel to the free stream direction, these forces are extracted for every portions of volume dividing the blade (see **Figure 3.7**). They will be named "X"and "Y" forces.

2/ For each volume, the angle β is calculated:

$$\beta = tan^{-1}\frac{U_\infty(1-a)}{R\omega(1+a')} \tag{4.3}$$

Where a is the axial induction factor and a' the tangential induction factor. The term $U_\infty(1-a)$ is actually the streamwise velocity value when arriving to the blade. $R\omega(1+a')$ is consequently, the tangential velocity. This formula is based on Blade Element Method (BEM) and the parameters a and a' were then difficult to evaluate accurately in the SRF study. For this case, $a'$was chosen = 0, and a = 0.25.

3/ Lift and Drag forces can be found using X and Y forces:

$$L = Ycos\,\beta + Xsin\beta \tag{4.4}$$

$$D = Ysin\,\beta - Xcos\beta \tag{4.5}$$

4/ The Angle of Attack (AOA) is determined by:

$$AOA = \beta - \varphi - \gamma \tag{4.6}$$

Where φ is the twist angle for each blade element, and γ the blade pitch angle (=0 for this case)

5/ Lift and Drag coefficients C_L and C_D are calculated following:

$$C_L, C_D = \frac{L, D}{\frac{1}{2}\rho[(U_\infty(1-a))^2 + (R\omega)^2]A} \tag{4.7}$$

Where R is the average radius of the blade element, ω the angular velocity and A is the planform area, which here was, the product of the average chord and the height of the blade element (fixed at 0.3m).

In terms of power for a 2 bladed turbine:

$$P = 2.X.z.\omega \tag{4.8}$$

Where z is the center of pressure of the blade, whose location is computed by ANSYS FLUENT, X is the "X" force.

Results and Discussion

Table 4.2. Power Output for different operating conditions

	$\boldsymbol{\omega}$ (rpm)	$\boldsymbol{U_\infty}$ (m/s)	T.S.R	Power (kW)	$\boldsymbol{\eta}$	Power from NREL (kW)
Case1	13.37	2	7	461	0.379	-
Case2	11.5	1.9	6.3	406.7	0.390	496.4
Case3	11.5	1.8	6.7	341.3	0.385	425.1
Case4	8.02	1.2	7	96.8	0.369	126.3

Table 4.2 summarizes the different simulations which were run at different operating conditions (free stream and angular velocity, both linked to TSR), the power output for each of them, the power efficiency based on the available kinetical power and the power output calculated by NREL. The latter has been computed based on 2D computation on all the NACA profiles composing the blade, which led to higher value (up to 30%) than the power based on our 3D computation. The following results might explain why such a gap was found.

Erreur ! Source du renvoi introuvable. presents the results of the followed methodology and the comparison with 2D results from the software XFOIL for each element of the blade, applied with the operating conditions corresponding to Case1 in **Table 4.2**. For XFOIL, a Reynolds Number $Re = 2.10^6$ was chosen. From left to right of the chart are displayed the blade elements from the root to the tip, with the related NACA profiles at the top, and the AOA values are mostly decreasing. See **Appendix C** for further details.

At the root, a very high value of drag and low lift coefficients can be observed, cause by the flow separation combined with the a non hydrodynamic shape of the section (ellipse). However, since the section shape is changing to a more and more common foil and that the AOA is high but still lower than the stall angle, the lift is increasing quickly (resp. the drag is decreasing) until it reaches its peak with the

profile 60247. Then comes a normal decrease involving the profile 60240 only, as the AOA decreases. Finally, close to the tip, C_L drops to 0.41 while the AOA stay relatively constant, and C_D remains steady.

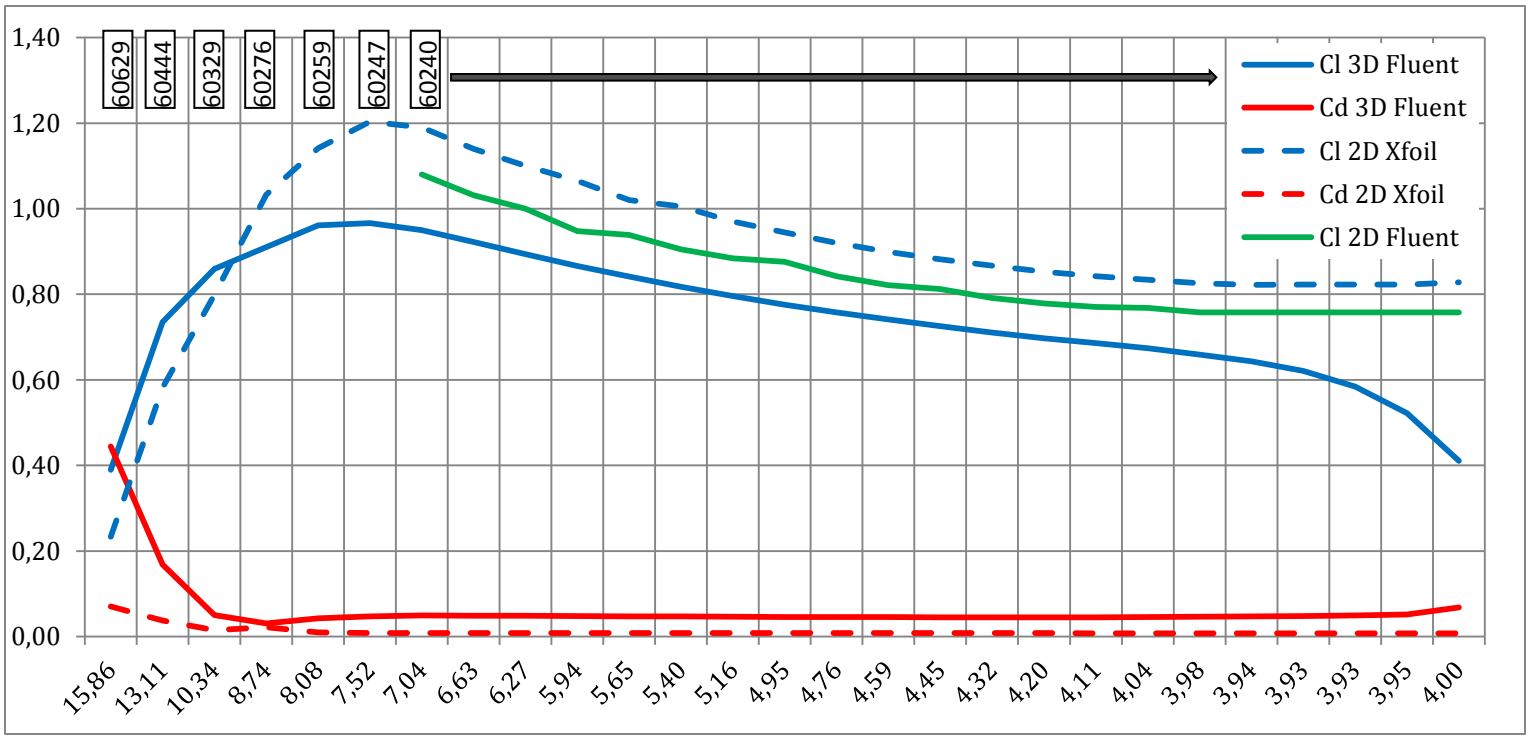

Figure 4.11. Lift and Drag Coefficients vs Angle of Attack (°) for the different sections of the blade

Again, the vortices shed by the tip of the blade, causing turbulent instabilities, are the reason of this drop of lift.

The overall 3D trend comparing to 2D results is about 23% lower on average for the lift coefficient, and 83% for the drag. The 2D data is, as expected from the theory, overestimating the performances of the blade, considering that 3D results are close to reality. Besides, this is a reason for the difference in Power output between our 3D computation and 2D computation from NREL in **Table 4.2.**

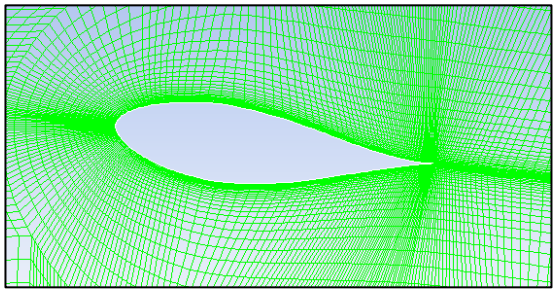

Figure 4.12. 2D mesh extracted from 3D model (section with 60240 NACA profile)

As to double-check the order of magnitude of both data, a simulation was run on ANSYS FLUENT 2D, using a section of the blade from the 3D initial mesh (see **Figure 4.12**). A C-based script was used to set the different boundary conditions, angle of attacks, write and post process the

data from FLUENT in a .txt file as to save time by automatizing these operations for a range of AOA.
It turned out that the obtained values for the correct AOA linked to the correct section was between 2D Xfoil and 3D FLUENT values, confirming the trend.

Nevertheless, even if the overall trend of lift and drag is correct, the determination of the AOA using the previous methodology, taken from BEM method, was not very accurate since it doesn't take into account 3D effects such as Coriolis or centrifugal forces. For example, the Coriolis force tends to change the direction of the component of the local velocity vector in the plane normal to the rotational axis. (16)
For a rotating blade, the flow passing by a blade section is bended due to the rotation of the rotor, and the local flow field is influenced by the bound circulation on the blade. Then, the corresponding term $U_\infty(1-a)$ in our methodology was difficult to evaluate.

A better method to determine the 3D AOA, both numerically and experimentally, can be found in (17). It consists in 4 steps to finally estimate to local velocity induced by the bound circulation. This procedure can be iterated or not.

5.CONCLUSION AND FUTURE WORK

Through the VBM study of an array of 8 turbines, using different spacing configurations, the assumptions made in the previous reports were confirmed. The influence of tip-to-tip distance, downstream distance and lateral offset are parameters influencing the capability of an array of turbine to extract power efficiently from kinetic energy transported by the flow. This data can be now used to predict with a reasonable accuracy the power a farm of MHK turbines can extract, based on the spacing configuration it has.

As to improve this accuracy, a future work could be to integrate the shear velocity profile in the model as to represent the seabed affecting the overall flow, and/or add more turbines as to test VBM on an industrial scale, by modifying the C-code to increment the maximum number of rotor in the VBM UDF (a modification has been made to enable 11 turbines but we didn't test it completely).

The methodology applied for our SRF study, including the division of the blade in several elements, getting the axial and radial forces in ANSYS FLUENT and using trigonometry and BEM method, led us to reasonable values of lift and drag coefficients and angle of attacks, and to a better knowledge of the behavior a blade in the near and far wake regions. However, the rotational effects inducing tip and root vortices and circulation modifying the flow field, need to be investigated more deeply, since we don't know if the actual procedure gave enough accuracy in the results or not.

A further study could also be to compare the 3D results with 2D from FLUENT, but with every sections of the blade as to get a reference dataset between 3D and 2D XFOIL and or keep only the upper parts of the blade as to avoid the shed vortices at the root and/or, once the lift and drag coefficients are calculated, to set them as an input for VBM as to estimate to power extraction capability of this turbine and its behavior in an array, for example. Besides, once the experiment will be conducted on the scaled prototype from which our geometry was based, comparisons between experimental and numerical data will be possible, as to confirm or improve our numerical model.

BIBLIOGRAPHY

1. **Rourke, F, Boyle, F and Reynolds, A.** Tidal energy update 2009. *Applied Energy.* 2010, 87, pp. 398-409.

2. **Fraenkel, P.** Tidal turbines harness the power of the sea. *Reinforced Plastics.* 2004, 48, pp. 44-47.

3. **Hall, T.** Numerical Simulation of a Cross Flow Marine Hydrokinetic Turbine. *Master's Thesis.* 2012.

4. **D., Hand M. and Jager D. Cotrell J. Schreck S. Larwood S. Simms.** *Unsteady aerodynamics experiment phase 6: Wind tunnel test configurations and available data campaigns.* 2001.

5. **F. Riesemann, M. Bewert.** *Array Optimization of Marine Hydrokinetic Turbine.* 2011.

6. **.Flouriot, A.Gosset and G.** *Optimization of Power Extraction in an array of Marine Hydrokinetic Turbines.* 2010.

7. **White, F. M.** Fluid Mechanics. 7th Edition. 2009, Chap 4.

8. **Pope, S. B.** Turbulent Flows. 2000, Chap 10: Turbulent-viscosity models.

9. http://www.cfd-online.com/Wiki/SST_k-omega_model. [Online]

10. **Zori, L.A.J., Rajagopalan, R.G.** Navier-Stokes Calculation of Rotor-Airframe Interaction in Forward Flight. *Journal of the American Helicopter Society.* April 1995, Vol. Vol.40.

11. **Fluent Inc.** ANSYS FLUENT 12.0 Theory Guide. 2009, Chap 2.2.1.

12. —. *UDF Manual.* 2006.

13. https://www.sharcnet.ca/Software/Fluent13/help/flu_ug/flu_ug_sec_bc_wall.html. [Online]

14. **Burton, T, et al., et al.** Wind Energy Handbook. s.l. : Wiley, 2001, Chap 3.

15. **Javaherchi, T.** Numerical Modeling of Tidal Turbines: Methodology Development and Potential Physical Environmental E. *Master's Thesis.* 2010, Chap 4.

16. **Carcangiu, C. E.** CFD-RANS Study of Horizontal Axis Wind Turbines. *PhD Thesis.* 2008.

17. **Shen, W. Z., Hansen, M. O. L. and Sorensen, J. N.** Determination of the Angle of Attack on Rotor Blades. *Wind Energy.* Wiley, 2008, pp. 91-98.

APPENDIX A: GEOMETRY OF THE NREL PHASE VI BLADE FOR THE VBM STUDY

Section number	Span Station (r/R)	Chord Length (m)	Twist angle (°)
1	0,25	0,7728	-18,074
2	0,273	0,711	-14,292
3	0,298	0,697	-11,909
4	0,353	0,666	-7,979
5	0,408	0,636	-5,308
6	0,424	0,627	-4,715
7	0,463	0,605	-3,425
8	0,518	0,574	-2,083
9	0,573	0,543	-1,15
10	0,576	0,542	-1,115
11	0,628	0,512	-0,494
12	0,683	0,482	0,015
13	0,727	0,457	0,381
14	0,739	0,451	0,475
15	0,794	0,42	0,92
16	0,849	0,389	1,352
17	0,864	0,381	1,469
18	0,904	0,358	1,775
19	0,959	0,328	2,191
20	1	0,305	2,5

APPENDIX B: GEOMETRY OF THE DOE REFERENCE MODEL 1

r/R	Radius	Pre-Twist	Chord	% Thick	Thickness	PitchAxis	Profile
(-)	(m)	(deg)	(m)	(t/c)	(m)	(x/c)	(-)
0,175	1,750	12,860	1,118	62,9	0,703	0,44	NACA6_0629
0,205	2,050	12,860	1,386	44,4	0,615	0,38	NACA6_0444
0,235	2,350	12,860	1,610	32,9	0,530	0,34	NACA6_0329
0,265	2,650	12,860	1,704	27,6	0,470	0,32	NACA6_0276
0,295	2,950	11,540	1,662	25,9	0,430	0,32	NACA6_0259
0,325	3,250	10,440	1,619	24,7	0,400	0,32	NACA6_0247
0,355	3,550	9,500	1,577	24	0,378	0,32	NACA6_0240
0,385	3,850	8,710	1,534	24	0,368	0,32	NACA6_0240
0,415	4,150	8,020	1,492	24	0,358	0,32	NACA6_0240
0,445	4,450	7,430	1,450	24	0,348	0,32	NACA6_0240
0,475	4,750	6,910	1,407	24	0,338	0,32	NACA6_0240
0,505	5,050	6,450	1,365	24	0,328	0,32	NACA6_0240
0,535	5,350	6,040	1,322	24	0,317	0,32	NACA6_0240
0,565	5,650	5,680	1,279	24	0,307	0,32	NACA6_0240
0,595	5,950	5,350	1,235	24	0,296	0,32	NACA6_0240
0,625	6,250	5,050	1,192	24	0,286	0,32	NACA6_0240
0,655	6,550	4,770	1,148	24	0,276	0,32	NACA6_0240
0,685	6,850	4,510	1,103	24	0,265	0,32	NACA6_0240
0,715	7,150	4,260	1,058	24	0,254	0,32	NACA6_0240
0,745	7,450	4,030	1,012	24	0,243	0,32	NACA6_0240
0,775	7,750	3,800	0,966	24	0,232	0,32	NACA6_0240
0,805	8,050	3,570	0,920	24	0,221	0,32	NACA6_0240
0,835	8,350	3,350	0,872	24	0,209	0,32	NACA6_0240
0,865	8,650	3,130	0,824	24	0,198	0,32	NACA6_0240
0,895	8,950	2,900	0,776	24	0,186	0,32	NACA6_0240
0,925	9,250	2,670	0,726	24	0,174	0,32	NACA6_0240
0,955	9,550	2,430	0,676	24	0,162	0,32	NACA6_0240
0,985	9,850	2,180	0,626	24	0,150	0,32	NACA6_0240

APPENDIX C: LIFT AND DRAG RESULTS FROM SRF SIMULATION

AOA (°)	Cl 3D Fluent	Cl 2D Xfoil	Cl 2D Fluent	Cd 3D Fluent	Cd 2D Xfoil
15,86	0,39	0,23	-	0,44417	0,07000
13,11	0,74	0,58	-	0,16831	0,03700
10,34	0,86	0,80	-	0,04982	0,01500
8,74	0,91	1,03	-	0,03041	0,02200
8,08	0,96	1,14	-	0,04237	0,01000
7,52	0,97	1,20	-	0,04729	0,00800
7,04	0,95	1,19	1,08	0,04939	0,00800
6,63	0,92	1,14	1,03	0,04893	0,00800
6,27	0,89	1,10	1,00	0,04837	0,00800
5,94	0,87	1,07	0,95	0,04784	0,00800
5,65	0,84	1,02	0,94	0,04728	0,00800
5,40	0,82	1,01	0,91	0,04691	0,00800
5,16	0,80	0,97	0,88	0,04638	0,00850
4,95	0,78	0,95	0,88	0,04597	0,00833
4,76	0,76	0,92	0,84	0,04550	0,00823
4,59	0,74	0,90	0,82	0,04527	0,00820
4,45	0,73	0,88	0,81	0,04501	0,00814
4,32	0,71	0,87	0,79	0,04485	0,00798
4,20	0,70	0,85	0,78	0,04466	0,00784
4,11	0,69	0,84	0,77	0,04511	0,00775
4,04	0,67	0,83	0,77	0,04563	0,00760
3,98	0,66	0,83	0,76	0,04607	0,00760
3,94	0,64	0,82	0,76	0,04680	0,00760
3,93	0,62	0,82	0,76	0,04788	0,00760
3,93	0,58	0,82	0,76	0,04920	0,00760
3,95	0,52	0,82	0,76	0,05125	0,00760
4,00	0,41	0,83	0,76	0,06778	0,00760